Microfluidic flow rate detection based on integrated optical fiber cantilever

Victor Lien and Frank Vollmer

Received 9th May 2007, Accepted 25th June 2007
First published as an Advance Article on the web 11th July 2007
DOI: 10.1039/b706944h

We demonstrate an integrated microfluidic flow sensor with ultra-wide dynamic range, suitable for high throughput applications such as flow cytometry and particle sorting/counting. A fiber-tip cantilever transduces flow rates to optical signal readout, and we demonstrate a dynamic range from 0 to 1500 μL min^{-1} for operation in water. Fiber-optic sensor alignment is guided by preformed microfluidic channels, and the dynamic range can be adjusted in a one-step chemical etch. An overall non-linear response is attributed to the far-field angular distribution of single-mode fiber output.

1 Introduction

There is perpetual demand in miniaturization and production-boost of biological/chemical laboratory processes, driven by availability of mass-productive and industrially-mature microfabrication technology. As an outcome, microfluidic technology, or so called ''lab-on-chip'', has already found numerous applications in chemical analysis and synthesis, sample preparation, mixing, particle sorting and droplet generation, just to name a few. High throughput applications such as flow cytometry and particle counting/sorting critically rely on the precise control of flow rates.[1–6] Therefore, there is a need for an integrated in-line flow sensor that can provide local and real-time feedback in complex lab-on-chip applications. Although sensitivity is the key issue, the sensor should also provide a wide and configurable dynamic range, since high throughput analysis of flow cytometry and particle counting/sorting uses flow rates which are much higher than those in applications, such as sample preparation and chemical synthesis.

In the development of microfluidic flow sensors, progress has been expedited by micro-electro-mechanical systems (MEMS) technology using detection schemes that rely on heat transfer,[7–12] drag-force or pressure induced changes in electrical parameters,[13–20] time-of-flight measurements of tracer chemicals,[21,22] flapping of a planar jet,[23] optical beam deflection[24] and other optical methods.[25] The sensor performances of MEMS devices are particularly impressive. Sensor architectures, however, are often complex[10,13,15,16,18,24,25] and fabrication is always a multi-step process that requires high-end fabrication tools and facilities, preventing their assembly and use in most biological and chemical laboratory settings.

Besides electrical or mechanical detection schemes, integration of optical fibers and other optical components with microfluidic devices may provide an alternative route to simple, yet highly sensitive flow sensors. Optical sensor techniques are particularly advantageous because of their resistance to chemical erosion and their non-invasive detection capability. One recent example is based on optical reflection from an air–water interface formed in a vertically opened microfluidic channel.[26] Although of high sensitivity, the dynamic range is limited (flow rate of nl s^{-1} to only several μl s^{-1}) and the operation relies on an unstable open channel design where the air–water interface may not reform after pressure spikes.

Here we present an integrated microfluidic fiber-optic flow-sensor with high sensitivity and ultra-wide dynamic range. Unlike most of the MEMS-based cantilever detection schemes which rely on electrical readouts or laser deflection, we take advantage of the mechanical flexibility and optical transparency of a silica optical fiber, the diameter of which can be thinned by hydrofluoric acid (HF) etching. The sensing mechanism is based on displacement of an emitting optical fiber-tip due to fluidic drag force, which reduces optical coupling to a receiving multi-mode fiber (Fig. 1a). Etching of the emitting fiber-tip cantilever can be controlled with micron-scale precision, which allows for precise adjustments of dynamic range.

2 Principle of operation

As shown in Fig. 1b, increase in volume flow rate bends the single-mode fiber-tip cantilever, which is then no longer aligned with the multi-mode receiving fiber, thus reducing the transmitted intensity. The drag force exerted on the fiber-tip cantilever with cylindrical cross-section is given as $F_D = \frac{1}{2}\rho A U^2 C_D$; where ρ is the density of fluid, U is the flow velocity, A is the cross-sectional area of the cylinder in the plane normal to U, C_D is the drag coefficient, and $A = 2aL$ in the case of a transverse cylinder of radius a and length L. The drag torque can be estimated from measured displacements of the fiber-tip due to the effective force F acting against the stiffness $Ea^4/4L^3$ of the cantilever, where $E \sim 63$ GPa is the Young's modulus of silica. Since the diameter of a standard single-mode fiber can be thinned by HF etching from 125 μm to less than 1 μm, the dynamic range for flow rate measurement is adjustable by several orders of magnitude.

When the fiber-tip cantilever is bent by fluidic drag force, the optical readout of the deflection displacement is directly obtained through fiber-to-fiber end-coupling. The single-mode fiber-tip is aligned with a cleaved multi-mode fiber and

Rowland Institute, Harvard University, 100 Edwin H. Land Blvd, Cambridge, MA, 02142, USA. E-mail: vollmer@rowland.harvard.edu; lien@rowland.harvard.edu; Fax: +16174974627; Tel: +16174974659

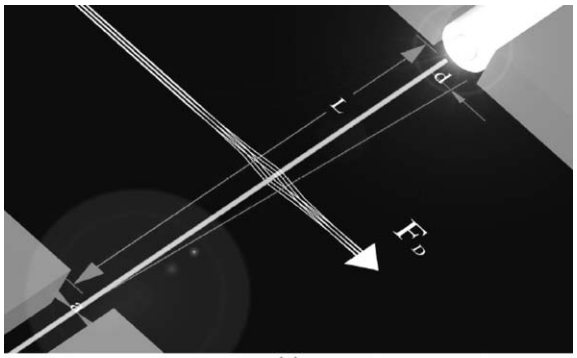

(a)

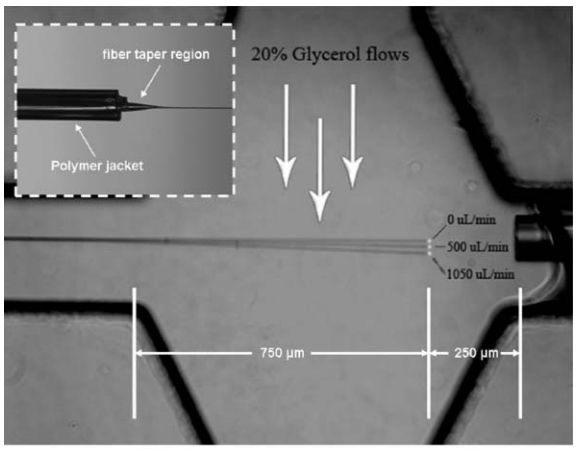

(b)

Fig. 1 Integrated micro-opto-fluidic flow sensor. (a) A stripped and thinned single-mode fiber (length L, diameter a) is positioned across a microfluidic channel and aligned with a multi-mode fiber which receives the emitted light. A laminar flow exerts a drag force F_D which displaces the fiber-tip by distance d, reducing the transmitted light intensity. (b) Micrograph of the flow sensor. Displacement of the fiber-tip is shown for three flow rates of a 20% glycerol–water mixture. The inset shows the fiber-tip cantilever fabricated in a one-step chemical etch.

permanently fixed in place during the fabrication process so that maximum coupling efficiency is obtained for zero flow rate. Fluidic drag force bends the cantilever (Fig. 1b), which results in a situation equivalent to an angular scan of the single-mode fiber's far-field distribution using a multi-mode fiber core as the detector (Fig. 2), assuming that the distortion of the fiber's fundamental mode field due to small-angle bending is negligible. In general, to calculate the far-field distribution E_f of light emitted from the fiber-tip, one can transform near-field distribution (guided mode), E, through Fraunhofer approximation (in cylindrical coordinates),

$$E_f(r,\theta) = \frac{j2\pi}{\lambda r}\exp(-jk_0 r)\int_0^\infty E(\rho')J_0(k_0\rho'\sin\theta)\rho' d\rho' \quad (1)$$

assuming independence of azimuthal angles φ and φ'.[27] Only the integral part determines the angular distribution of the electric far-field. Therefore,

$$|E_f(\theta)| = \int_0^\infty E(\rho')J_0(k_0\rho'\sin\theta)\rho' d\rho' \quad (2)$$

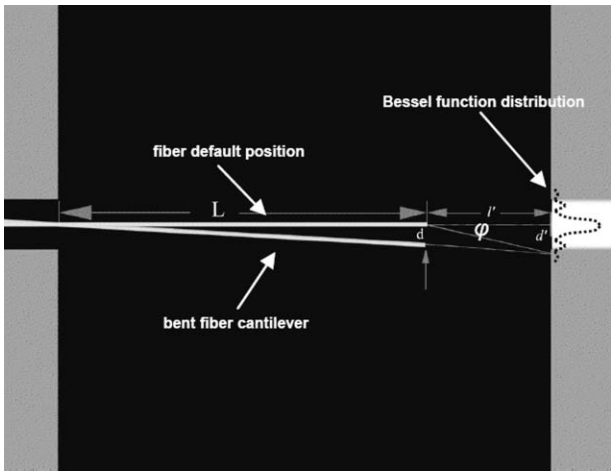

Fig. 2 Intensity distribution of optical readout. The far-field intensity distribution projected on the core of the receiving fiber is described by Bessel functions.

where $E(\rho')$, the near-field distribution of a single-mode fiber, is the solution of the well-known Helmholtz equation in a cylindrical coordinate system,

$$E(\rho') \propto J_l(k\rho'),\ \rho' < a \text{ (core) } K_l(\gamma\rho'),\ \rho' > a \text{ (cladding)} \quad (3)$$

where J_l is the Bessel function of first kind and order l, and K_l is the modified Bessel function of the second kind and order l. By substituting solution (3) into eqn (2), we can calculate the angular distribution of far-field power intensity,

$$P(\theta) \propto |E_f(\theta)|^2 = \left| \int_0^a J_0(k\rho')J_0(k_0\rho'\sin\theta)\rho' d\rho' + \int_a^\infty K_0(\gamma\rho')J_0(k_0\rho'\sin\theta)\rho' d\rho' \right|^2 \quad (4)$$

In other practical applications, the far-field angular distribution is commonly approximated by a Gaussian function. It is also known that the angular field distribution of single-mode fibers resemble Gaussian functions to a superior accuracy for practical approximation.[28]

The far-field image shifts by angle φ due to the fiber cantilever's response to flow. Therefore, $P(\theta)$ translates to $P(\theta-\varphi)$. The change of intensity I of the sensor readout with varying angular displacements φ is given by,

$$I(\varphi) = \int_{-\theta_a}^{\theta_a} P(\theta-\varphi)d\theta = \int_{-\theta_a}^{\theta_a} \left| \int_0^a J_0(k\rho')J_0(k_0\rho'\sin(\theta-\varphi))\rho' d\rho' + \int_a^\infty K_0(\gamma\rho')J_0(k_0\rho'\sin(\theta-\varphi))\rho' d\rho' \right|^2 d\theta \quad (5)$$

where θ_a is the multi-mode fiber acceptance angle given by $\sin^{-1}NA$, where NA stands for numerical aperture. As we mentioned earlier, signal readout for various flow rates is the equivalent to a profile scan of the far-field distribution of a single-mode fiber (fiber cantilever), with a multi-mode fiber

(receiver). It is worth to note that the angle φ in the above equations is not defined as the bending angle of the fiber cantilever. Instead, it is defined (Fig. 2) as $\varphi = \tan^{-1}(d'/l')$, where d' is the displacement of the far-field image, l' is the gap between the aligned fiber ends, and $d' = d(L + l')/L$.

3 Experiments

The sensor is assembled by aligning a single-mode optical fiber (8.2 μm core diameter, SMFe-28 Corning) and a multi-mode optical fiber (62.5 μm core diameter, CPC6 Corning, Fig. 1a). Both fibers are stripped from their polymer sheet (250 μm jacket diameter) only at the ends where the 125 μm diameter cladding (including core) is exposed. Alignment is guided by the microfluidic channel structure molded by soft lithography in polydimethylsiloxane (PDMS). The two fibers are threaded through two ~300 μm wide alignment channels, so that the stripped part of the single-mode fiber crosses the 750 μm wide microfluidic channel (Fig. 1b). In this example, a gap of 250 μm is formed between the aligned ends of the single- and multi-mode fiber. All channels are 250 μm high and are replica molded from SU-8 micro-structures. The PDMS slab is covalently bonded to a glass slide by oxygen plasma treatment. Permanent fiber alignment is achieved using UV-sensitive adhesive (Norland), introduced in alignment channels by capillary forces and cured as it reaches the channel junction (Fig. 1b). To reduce scattering from the tapered single-mode fiber region, the adhesive is mixed with a small amount of silver paint. Before assembly, the tip of the single-mode fiber is thinned in a one-step chemical etch using 50% HF acid at 60 °C (inset Fig. 1b). Before immersion in HF, the polymer jacket of the single-mode fiber has been carefully stripped, and the fiber is cleaved to expose just the right length of unsheathed fiber. The etching progress is monitored through a 4× telescope (Rolyn Optics) and terminated by rinsing in distilled water. After 25 min of etching, the fiber-tip was thinned to a final diameter of 9 μm. Removal of the fiber cladding does not interfere with light-guidance through the core (refractive index $n \sim 1.468$), since the lower refractive index cladding ($n \sim 1.463$) is replaced by water ($n = 1.333$).

In our experimental setup, flow is driven by a syringe pump (Model PHD 22/2000, Harvard Apparatus). A disposable syringe was connected to the microfluidic channel through Teflon tubing and an on-chip connector. A DFB (distributed feedback) laser of 1550 nm nominal wavelength (Anritsu GB5A016) was used as a light source and coupled into the single-mode fiber. The output optical signal was detected by an amplified, switchable-gain, InGaAs detector (Thorlabs Inc. PDA400) and recorded in real-time by data acquisition software (Labview). In principle, the flow sensor can be operated at arbitrary wavelengths.

4 Results and discussion

Fig. 3 shows the optical readout of the fiber cantilever sensor in response to various flow rates of distilled water. It is seen that the sensor recovers its baseline response even after transient exposure to relatively large flow rates.

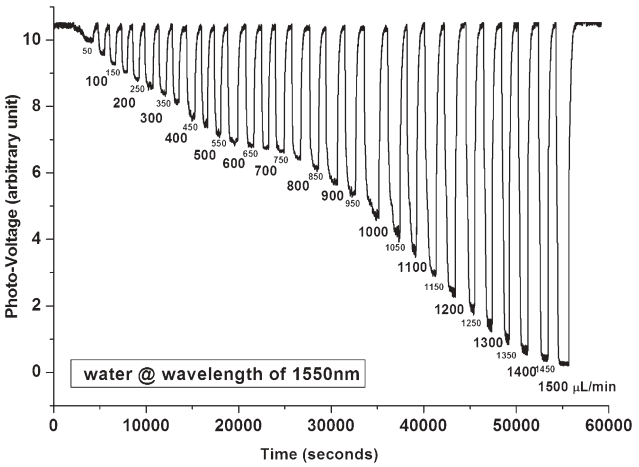

Fig. 3 Optical response of the fiber cantilever sensor to various volumetric flow rates (0–1500 μL min^{-1}) of water, measured at 1550 nm wavelength.

Similar experiments are performed for glycerol–water solutions with varying viscosity (Table 1). The average normalized intensity values are plotted *versus* volumetric flow rates in Fig. 4.

In all experiments, the background noise remains approximately at the same level. Dividing the background noise level by total intensity gives the sensing resolution at ~0.022. As seen from Fig. 4 and Table 1, besides flow rate, the sensor response also depends on viscosity, which determines the drag force at a given flow velocity. It is also seen that the response is non-linear, resulting in sensitivity that varies with flow rate. To

Table 1 Physical properties of glycerol–water solutions

Volume%	Mass%	Density, ρ/g cm^{-3}	Refractive index, n	Viscosity, η/mPa s^{-1}
D.I. water	0	1	1.3334	1
10% glycerol	12.29%	1.0269	1.3475	1.382
20% glycerol	23.97%	1.0560	1.3624	1.989
40% glycerol	45.67%	1.1137	1.3919	4.868

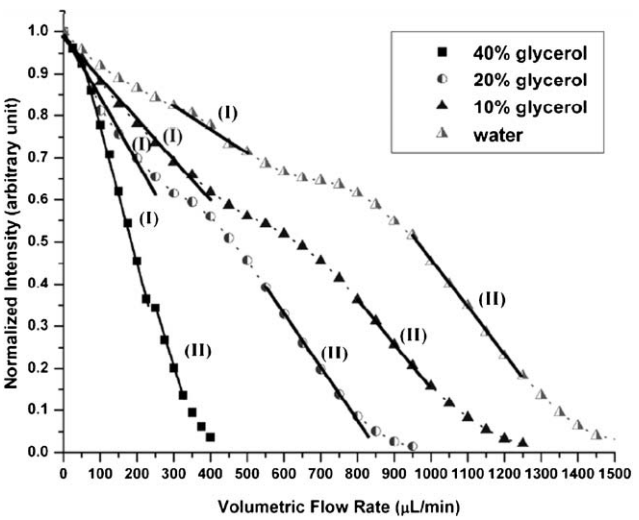

Fig. 4 Sensor response to flow rates of fluids with varying viscosity

Table 2 Sensitivity in selected flow rate regions I and II

Selected region		(I)	(II)
D.I. water	Flow rate range	300–500 μL min^{-1}	950–1250 μL min^{-1}
	Minimum detectable	31 μL min^{-1}	18 μL min^{-1}
10% glycerol	Flow rate range	0–400 μL min^{-1}	800–1000 μL min^{-1}
	Minimum detectable	23 μL min^{-1}	21.8 μL min^{-1}
20% glycerol	Flow rate range	0–250 μL min^{-1}	550–850 μL min^{-1}
	Minimum detectable	17.7 μL min^{-1}	18.1 μL min^{-1}
40% glycerol	Flow rate range	50–225 μL min^{-1}	275–325 μL min^{-1}
	Minimum detectable	6.1 μL min^{-1}	7.7 μL min^{-1}

estimate sensitivity, we fit linear functions to each of the two quasi-linear regions (labeled I and II) identified in the sensor response (Fig. 4). We divide the sensing resolution (0.022) by the slope of the linear fits to obtain the minimal detectable flow rates in regions I and II (Table 2).

To determine the origin of non-linearity, we measured the deflection of the fiber-tip for various volumetric flow rates and fluidic viscosities by recording the fiber-tip position using a charge-coupled device camera mounted on a microscope (Fig. 1b). Shown in Fig. 5 are the curves for the mechanical displacement of the fiber-tip *versus* flow rate, which are smooth and therefore can not explain the non-linear optical response (Fig. 4).

Instead, we attribute the non-linear optical response to the far-field distribution of light that is emitted from the fiber-tip (eqn (4), the far-field distribution is illustrated in Fig. 2). The distribution contains side-lobes due to the presence of Bessel functions that describe the near-field (eqn (1)–(3)).[28] We can calculate the sensor response by taking the integral of the far-field distribution over the diameter of the receiving multi-mode fiber core for different angular displacements of the cantilever (eqn (4)). The resulting total transmitted intensity *versus* angular displacement is plotted in Fig. 6. In the calculation, we use the parameters summarized in the experimental section, assume a water cladding and $NA = 0.479$ for the receiving fiber. Also plotted in Fig. 6 are measurements of fiber transmission *versus* cantilever displacement as determined from micrographs, such as Fig. 1b, as well as intensity values expected for a Gaussian far-field distribution.[28] From overlap of simulation results and experimental data we find that the position of inflection points (dashed vertical lines) can be predicted quite accurately. The difficulty in fitting the overall sensor response suggests that the actual amplitudes in the far-field pattern differ from predictions based on eqn (2). The deviation may be due to eccentricity of the single- and multi-mode fiber core and due to scattering. Furthermore, we approximated the 2D circular aperture of the multi-mode fiber in one dimension.

The non-linear response is undesirable and could be avoided by operating in one of the two quasi-linear flow rate regimes identified in Fig. 4. Use of triangular-graded single-mode fibers may provide a linear sensor response since the far-field angular distribution is expected to be linear.[27]

Cantilevers of higher sensitivity can be fabricated by further thinning diameter a and increasing length L so that displacement d is maximized according to:

$$d \propto \frac{4L^4 \rho U^2 C_D}{Ea^3} \tag{6}$$

The ultimate sensitivity is set by material properties of the fiber cantilever because if fabricated too thin at certain length, the cantilever will bend under its own weight and might stick to the channel wall during sensor assembly. Also, a thinner

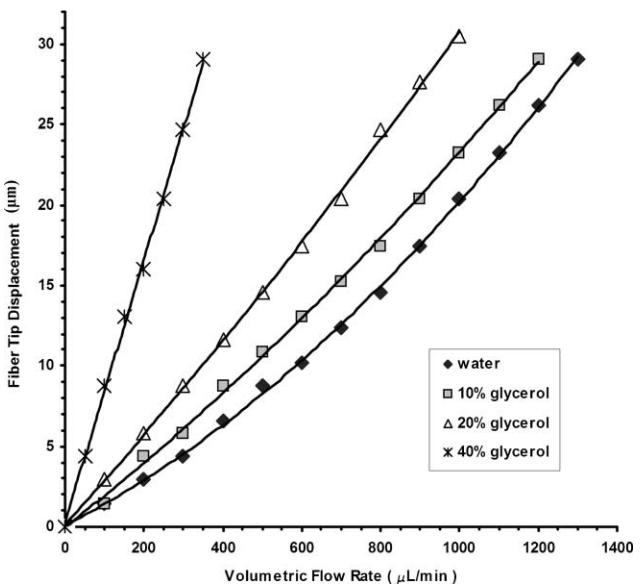

Fig. 5 Mechanical response of fiber cantilever. The deflection displacement of the fiber-tip for various volumetric flow rates and viscosities was measured under a microscope. The lines are quadratic curve fits.

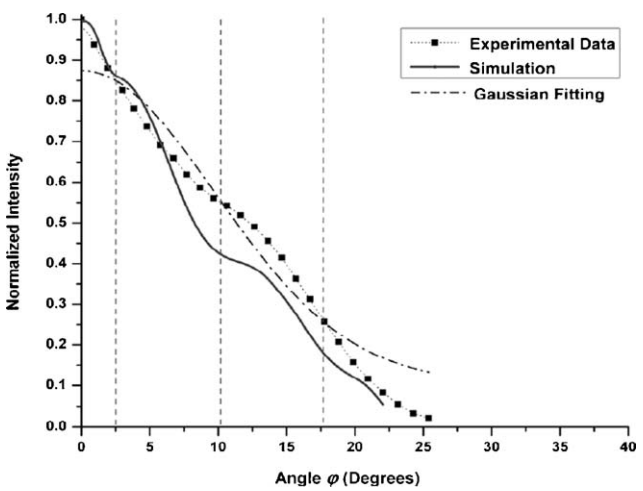

Fig. 6 Calculated and measured sensor response as function of angular cantilever displacement.

cantilever has a smaller dynamic range which is set by the numerical aperture of the receiving fiber and by the gap between the aligned fiber ends. A larger dynamic range could be obtained by alignment of two or more receiving fiber ends.

One practical problem during sensor operation is the issue of fouling. Small particles deposited on the surface of the cantilever will increase drag force which results in a larger displacement. The problem can be avoided by filtering of the fluid or by appropriate chemical treatment of the silica material. On the other hand, this issue might provide a new mechanism for detection of cells, bacteria, viral particles or other contaminants to the flow.

5 Conclusions

To summarize, we demonstrate an integrated micro-opto-fluidic flow-sensor with high sensitivity and large dynamic range which can be adjusted in a one-step chemical etch. A fiber cantilever transduces flow rate into optical transmission signals. Using a 9 μm diameter cantilever, we show a dynamic range $\sim$0–1500 μL min^{-1} for operation in water. The minimum detectable flow rate is measured at $\sim$7 μL min^{-1} for viscosity at 4.868 mPa s^{-1}. The nonlinear response of the optical readout is attributed to the far-field angular distribution of light emitted by the single-mode fiber. Triangular-graded fibers are suggested for future applications that require a linear sensor response. Etching of a thinner and longer fiber cantilever can increase sensitivity, however, there is a design trade-off between sensitivity and dynamic range. The problem of fouling can be avoided by the filtering of samples, but may also provide a novel detection mechanism for particles that contaminate the flow.

Acknowledgements

This work was supported by the Rowland Junior Fellowship program and was performed in part at the Center for Nanoscale Systems at Harvard (CNS), which is supported by the National Science Foundation under NSF award no. ECS-0335765. We thank Jun Zhang (Courant Institute, NYC) for critical reading of the manuscript.

References

1 V. Lien, K. Zhao and Y.-H. Lo, *IEEE J. Sel. Top. Quantum Electron.*, 2005, **11**, 827–834.
2 V. Lien, K. Zhao and Y.-H. Lo, *Appl. Phys. Lett.*, 2005, **87**, 1941061–3.
3 J. Godin, V. Lien and Y.-H. Lo, *Appl. Phys. Lett., 2006*, 2006, **89**, 0611061–3.
4 A. Y. Fu, C. Spence, A. Scherer, F. H. Arnold and S. R. Quake, *Nat. Biotechnol.*, 1999, **17**, 1109–1111.
5 A. Wolff, I. R. Perch-Nielsen, U. D. Larsen, P. Friis, G. Goranovic, C. R. Poulsen, J. P. Kutter and P. Telleman, *Lab Chip*, 2003, **3**, 22–27.
6 Y.-C. Tung, M. Zhang, C.-T. Lin, K. Kurabayashi and S. J. Skerlos, *Sens. Actuators, B*, 2004, **98**, 356–367.
7 M. Ashauer, H. Glosch, F. Hedrich, N. Hey, H. Sandmaier and W. Lang, *Sens. Actuators*, 1999, **73**, 7–13.
8 H.-E. de Bree, P. Leussink, T. Korthorst, H. Jansen, T. S. J. Lammerink and M. Elwenspoek, *Sens. Actuators, A*, 1996, **54**, 552–557.
9 F. J. M. van der Eerden, H.-E. de Bree and H. Tijdeman, *Sens. Acutators, A*, 1998, **69**, 126–133.
10 S. Wu, Q. Lin, Y. Yuen and Y.-C. Tai, *Sens. Actuators, A*, 2001, **89**, 152–158.
11 A. Glaninger, A. Jachimowicz, F. Kohl, R. Chabicovsky and G. Urban, *Sens. Actuators*, 2000, **85**, 139–146.
12 J. Chen, Z. Fan, J. Zou, J. Engel and C. Liu, *J. Aerospace Eng.*, 2003, **16**, 85–97.
13 M. Dijkstra, J. J. van Baar, R. J. Wiegering, T.S.J. Lammerink, J. H. de Boer and G. J. M. Krijnen, *J. Micromech. Microeng.*, 2005, **15**, S132–138.
14 A. Quist, A. Chand, S. Ramachandran, D. Cohen and R. Lal, *Lab Chip*, 2006, **6**, 1450–1454.
15 R. E. Oosterbroek, T. S. J. Limmerink, J. W. Berenshot, G. J. M. Krijnen, M. C. Elwenspoek and A. van den Berg, *Sens. Actuators*, 1999, **77**, 167–177.
16 G. J. M. Krijnen, M. Dijkstra, J. J. van Baar, S. S. Shankar, W. J. Kuipers, R. J. H. de Boer, D. Altpeter, T. S. J. Lammerink and R. Wiegerink, *Nanotechnology*, 2006, **17**, S84–89.
17 Z. Fan, J. Chen, J. Zou, D. Bullen, C. Liu and F. Delcomyn, *J. Micromech. Microeng.*, 2002, **12**, 655–661.
18 S. Radhakrishnan and A. Lal, *J. Microelectromech. Syst.*, 2005, **14**, 1013–1022.
19 J. Collins and A. P. Lee, *Lab Chip*, 2004, **4**, 7–10.
20 J. Lee, K. Naeli, H. Hunter, J. Berg, T. Wright, C. Courcimault, N. Naik, M. Allen, O. Brand, A. Glezer and W. P. King, *Sens. Actuators, A*, 2007, **134**, 128–139.
21 J. Wu and W. Sansen, *Sens. Actuators, A*, 2002, **97–98**, 68–74.
22 J. Wu and J. Ye, *Lab Chip*, 2005, **5**, 1344–1347.
23 G.-B. Lee, T.-Y. Kuo and W.-Y. Wu, *Exp. Therm. Fluid Sci.*, 2002, **26**, 435–444.
24 D. A. Czaplewski, B. R. Ilic, M. Zalalutdinov, W. L. Olbricht, A. T. Zehnder, H. G. Craighead and T. A. Michalske, *J. Microelectromech. Syst.*, 2004, **13**, 576–585.
25 P. Norlin, O. Oehman, B. Ekstroem and L. Forssen, *Sens. Actuators, B*, 1998, **49**, 34–39.
26 L. Szekely, J. Reichert and R. Freitag, *Sens. Actuators, A*, 2004, **113**, 48–53.
27 M. V. Grekov, S.A. Vasil'ev, I. G. Korolev, A. S. Boshkov, O. I. Medvedkov and A. K. Senatorov, *Instrum. Exp. Tech.*, 2005, **48**, 96–101.
28 A. T. Klemas, D. S. Shenk, W. A. Reed and M. A. Saifi, *J. Lightwave Technol.*, 1985, **3**, 967–970.

